

Permeability of Single-Layer-Free-Standing Meshes at Varying Capillary Pressure via a Novel Method

Muhammad R. Shattique, Roman Giglio, Ercan M. Dede, Sreekant Narumanchi, Mehdi Asheghi, Kenneth E. Goodson, and James W. Palko*

The permeability of mesh wicks is important for various applications, including two-phase heat transfer. However, the understanding of the permeability of single-layer, free-standing mesh wicks, with liquid–gas interfaces on both sides, is limited. A novel and simpler method is presented to determine the permeability of a free-standing wick and apply it to a representative mesh. This method involves modifying the capillary pressure via elevation and simultaneously measuring the permeability to determine the permeability–capillary pressure relationship. When applied to a copper mesh with plain weave having undergone surface cleaning, the permeability is found to decrease as capillary pressure for deionized water increases. A dimensional analysis is presented to generalize this data for other mesh sizes with similar weaves and fluids. The behavior of mesh in application is modeled, based on the integration of Darcy’s law with an analytic function fit to measured data, and parametric studies are conducted to investigate the superficial velocity of liquids through the mesh under varying driving pressures, transport lengths, and liquid viscosity, based on the obtained capillary pressure–permeability relationship. This study provides valuable insights into the transport properties of mesh wicks, with potential applications in fields such as electronics cooling, electrochemical devices, and fluid purification technologies.

transferring fluids by capillary action. Their low flow resistance allows transfer of fluids over long distances with minimal pressure drop, making them useful in systems that require a low-pressure gradient, such as heat pipes and fuel cells.^[1] In addition, mesh wicks can also be found in oil–water separation systems, desalination systems and gas separation systems.^[2–5] As an important example application, in two-phase heat transfer systems, it is often necessary to maintain a thin film of evaporating liquid on the surface of a porous matrix in order to enhance heat transfer.^[6–9] This enhancement can be achieved using a mesh wick, transporting the liquid through capillary action without needing external pumping. The capillary action of the wick can increase the heat transfer coefficient and the critical heat flux in evaporation and boiling heat transfer processes through optimal delivery of coolant fluid to the heated area.^[10–13]

The permeability of a mesh wick refers to its ability to allow fluids to pass through it. It is influenced by the


size and shape of the pores in the wick, and when multiple, immiscible phases are present, the surface tension of the liquids and surface energy of the matrix and the relative pressure within each phase.^[14–17,18] The permeability of a mesh can be an important factor in many applications, as it can affect the rate at which fluids are transferred through the wick. Darcy’s law is used to

1. Introduction

Porous materials, such as mesh wicks, can transport mass, charge, and energy through their pores and matrix and enhance interaction between these two spaces due to their high surface area. Mesh wicks are commonly used in various applications for

M. R. Shattique
 Materials and Biomaterials Science and Engineering
 University of California
 Merced, CA 95343, USA

R. Giglio, J. W. Palko
 Mechanical Engineering
 University of California
 Merced, CA 95343, USA
 E-mail: jpalko@ucmerced.edu
 E. M. Dede
 Electronics Research Department
 Toyota Research Institute of North America
 Ann Arbor, MI 48105, USA
 S. Narumanchi
 National Renewable Energy Laboratory
 Golden, CO 80401, USA
 M. Asheghi, K. E. Goodson
 Mechanical Engineering
 Stanford University
 Stanford, CA 94305, USA

 The ORCID identification number(s) for the author(s) of this article can be found under <https://doi.org/10.1002/admi.202300326>

© 2023 The Authors. Advanced Materials Interfaces published by Wiley-VCH GmbH. This is an open access article under the terms of the Creative Commons Attribution License, which permits use, distribution and reproduction in any medium, provided the original work is properly cited.

DOI: 10.1002/admi.202300326

describe the flow of a fluid through a porous medium based on pressure gradient, ∇p , and dynamic viscosity of the fluid, μ .^[19]

$$u = -\frac{k_i k_r}{\mu} \nabla p \quad (1)$$

The superficial velocity, u , is equal to the volumetric flow rate (Q) divided by the cross-sectional area (A) of the face of the media normal to the flow. $A = \text{width } (w) \times \text{thickness } (\delta)$. In a free-standing mesh, the cross-sectional area for flow is ambiguous, but the superficial velocity can be normalized by the thickness of the single layer of mesh matrix to give $u\delta = Q/w$.

In (1), k_i and k_r are intrinsic and relative permeabilities, respectively. Intrinsic permeability is a fundamental parameter related to the geometry of the porous medium and it scales with the square of the characteristic feature size. It has dimensions of area and is often expressed in units of m^2 , or non-SI units, such as Darcy (Da). Relative permeability is dimensionless and defined as the ratio of superficial velocity of a given fluid when another immiscible fluid is also present to the value when only the original given fluid is present. The relative permeability depends on the porous structure as well as on the participating fluids and the present and past conditions of the system. The relative permeability of a fluid in a porous medium exhibits a saturation dependency, with a decrease in relative permeability as saturation decreases. In turn, saturation (and therefore permeability) exhibits a dependency on capillary pressure, which may show considerable hysteresis. The Gardner, van Genuchten-Mualem model, Brooks–Corey–Burdine model and theory proposed by Papatzacos–Skjæveland, are commonly employed in analytical and numerical modeling of these properties.^[20–22] For thin, porous structures without well-defined internal pores, such as free standing meshes, the meaning of relative permeability is less clearly defined and the dependence on flow resistance with capillary pressure less well known.

To measure in-plane intrinsic permeability of meshes, researchers have developed methods considering stacks of meshes submerged in a liquid to understand how different characteristics of the mesh, such as the number of layers, wire diameter and spacing, crimping factor, mesh thickness, and stacking density, can influence single-phase flow through the mesh.^[23–30] The results of these studies have contributed to the development of models, such as the modified Blake–Kozeny equation, which can predict the intrinsic permeability of metal meshes for certain configurations. However, both the measurement methods and mathematical models may not be accurate for very thin stacks of mesh and do not address meshes with free surfaces. The mesh structure and the surrounding environment also affect how liquid flow resistance varies as capillary pressure changes. Some studies have considered flow in meshes with free surfaces, such as the configuration used in the study by Si-Cong Tan et al.^[31] In this study, the permeability of an ultra-thin screen wick with a free surface on one side of the mesh was investigated using a gravity flow method. The copper meshes were welded to a copper plate, leaving a vapor–liquid interface on one side, and the liquid was pumped into the wick using a microflow pump. However, the method is not suitable to measure the permeability of free-standing meshes with liquid-vapor interface on both sides. Additional studies have measured in-plane relative permeability

of thin, porous films.^[13,32] The environment can play a role in the fluid flow properties of woven meshes, particularly through its effect on evaporation from the wick.^[33] Changes in temperature and relative humidity can alter the radius of curvature of the liquid–vapor interface as described by the Kelvin equation.^[34] Models have also been developed for through-plane single-phase permeability of meshes accounting for the full 3D structure.^[35]

Above a certain capillary pressure in a given porous structure, a percolating liquid phase no longer exists and the relative permeability drops to zero.^[36] Smaller pores and higher surface tension result in higher values of this maximum allowable capillary pressure. Optimizing the tradeoff between resistance to capillary pressure and high intrinsic permeability allows enhanced performance in liquid wicking applications.^[37] Maximum capillary rise, capillary rate of rise, and bubble point measurements may be used to approximate this maximum allowable capillary pressure.^[36,38–40]

In this study, we demonstrate a new, simple method to measure the permeability of free-standing mesh structures that have liquid-vapor interfaces on both sides. The method involves liquid capillary suction through the mesh by fixing a driving force of gravitational potential using water pools at different heights. It allows measurement of permeability at different capillary pressures. We measure the relationship between permeability–thickness–product ($k\delta$) and capillary pressure in free-standing #100 copper mesh wicks. We provide dimensional analysis to extend the results to other mesh sizes and materials with similar weaves and different working fluids. To our knowledge, the capillary pressure dependence on the liquid permeability of thin single layer porous structures, such as mesh wicks, that are exposed to vapor phases on both sides has not been previously determined. The relationship between $k\delta$ and capillary pressure of a single layer free-standing mesh can be used to calculate the overall flow performance in various situations by integrating Darcy's law and can be helpful in the design of mesh-based microfluidic devices for two-phase heat transfer applications.^[41]

2. Experimental Section

2.1. Mesh

Metal mesh formed from copper with 99.9% purity (McMaster-Carr) was analyzed. The mesh had a plain weave, **Figure 1a**, with 100 wires per linear inch, opening size of 0.152 mm, wire diameter, D , of 0.114 mm, and 30.3% open area. The thickness of the mesh, δ , was 0.280 mm. A scanning electron microscope (SEM) image of the mesh, **Figure 1b**, revealed that the weave created square openings with all wires of generally uniform size. The mesh showed fourfold symmetry with wires in both orientations being similarly deformed.

2.2. Methods

2.2.1. Chemical Surface Preparation of Copper Mesh

As received, the copper mesh carried surface contamination. Prior to permeability characterization, the mesh was cleaned in caustic solution and then etched in acidic solution to insure

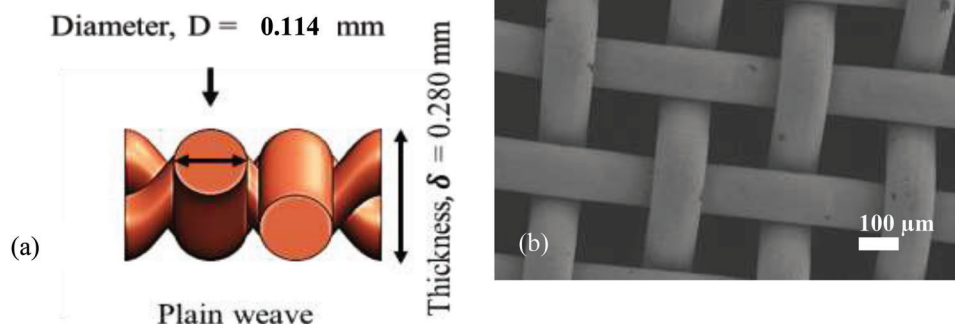


Figure 1. Geometry and dimensions of copper wire mesh, a) rendering of mesh with wire diameter, $D = 0.114$ mm, and thickness, $\delta = 0.280$ mm. The mesh has a plain weave. b) SEM image.

Table 1. Surface preparation steps for copper mesh samples..

Step number	Process description
1	Cleaning with Deionized (DI) water for 15 min
2	Cleaning in 1 M NaOH for 40 min at 80 °C
3, 4, 5	Cleaning with DI water for 5 min
6	Etching in 1% H ₂ SO ₄ for 80 min at 80 °C
7, 8, 9	Cleaning with DI water for 5 min

reproducible surface properties. The steps for the surface preparation process are listed in **Table 1**. 1 M NaOH was prepared from NaOH pellets (MDL Number: MFCD00003548) having 97% purity. 1% H₂SO₄ was prepared from concentrated (95–98%) H₂SO₄ (MDL Number: MFCD00064589).

This preparation protocol resulted in consistent data for permeability and capillary rise. Cleaning with surfactants and solvents including hexane and acetone was also explored but found this approach to yield inconsistent results.

2.2.2. Imaging

The surface of the copper wire mesh was imaged using an SEM (Zeiss Gemini SEM 500), Figure 1b, with 3 kV accelerating voltage and Everhart Thornley secondary electron detector.

2.2.3. Permeability Experimental Set-Up

Figure 2a shows a schematic of the permeability measurement set-up. In essence, the mesh formed a siphon between two pools. Two side by side mesh siphons were considered in each setup (Figure 2c). The samples had the same length in the vertical sections but different lengths in the horizontal sections. Comparison of the resistance between the two samples allowed approximate isolation of resistance due to the excess horizontal section in the longer sample (L^* in Figure 2d). Permeability of the section L^* was measured at varying capillary pressure.

The two water pools were maintained at heights h_1 and h_2 , respectively, where $h_1 > h_2$. The pool height difference, $h = h_1 - h_2$ was kept constant throughout all experiments at 4.7 cm. Each copper mesh was folded to create three sections. A vertical section

rose from the top water pool (with length l_u), a horizontal section bridged the two pools (l_x), and a second vertical section dropped to the lower pool (l_l). It was ensured that the mesh was fully saturated in deionized (DI) water prior to each experiment by submerging the mesh in a bath of DI water for 10 min. As the mesh was initially saturated, the experiment occurred in a drainage mode. No significant difference was expected in behavior if the mesh approached steady state from an unsaturated condition, but this condition was not tested, and imbibition into the mesh was very slow. During the experiment, DI water was siphoned from the upper pool through the horizontal section to the lower pool due to the difference in gravitational potential. The capillary pressures in the horizontal sections of the mesh could be controlled by changing their height with respect to the water pools. An environmental control chamber, with wicking humidifier, maintained an atmosphere that was nearly saturated with water vapor during experiments. Humidity was monitored throughout the experiment using electronic humidity sensors (HTM2500LF, Humidity measuring range(%RH): 0–100, humidity sensor assembly accuracy (%RH): ± 3). A secondary cover over the experimental samples prevented the possibility of any condensation from the outer casing falling on the samples themselves.

Detailed calculations allowing determination of permeability are discussed in the subsequent section. A key element allowing determination of permeability at a defined capillary pressure was the use of two samples in each experiment, as seen in Figure 2b. The two samples had the same vertical wicking lengths from the upper pool (l_u) and lower pools (l_l), respectively, which could be adjusted, Figure 2c. However, the length of their horizontal sections (l_x) was different, as pointed out in Figure 2d. $l_1 = 8$ cm and $l_2 = 16$ cm. l_1 and l_2 were kept constant throughout all experiments. The width of the copper mesh strips was 4 cm. This width minimized edge effects and had been used in recent studies of permeability of mesh with a single free surface.^[31]

2.3. Experimental Procedure

2.3.1. Permeability of Copper Mesh

After cutting the meshes, they were cleaned following the protocol described above. The meshes were then dipped into a DI water pool to saturate them entirely. At the beginning of each

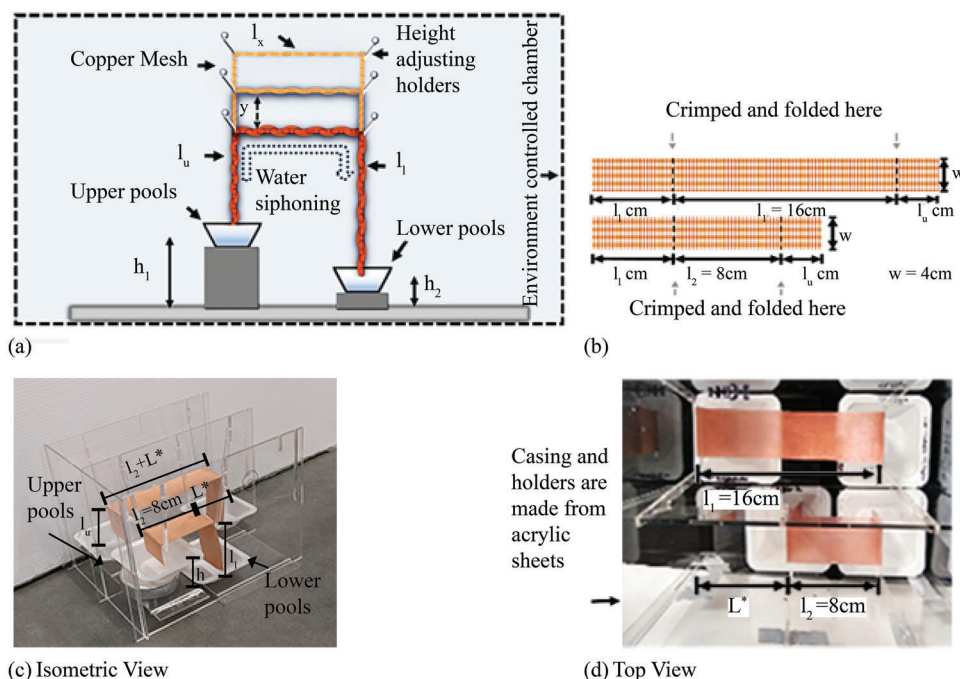


Figure 2. a) Schematic of the experimental set-up for permeability measurements. Water is siphoned from the upper pool to the lower pool via capillary action of the mesh. b) Schematic of mesh sections with their dimensions. Meshes are crimped and folded at the dotted lines to create three sections, two vertical (l_u and l_l) and one horizontal ($l_x = l_1$ or l_2). c) Isometric view of the setup: the vertical lengths (l_u and l_l) are equal for both the meshes. The pool height difference, h , between the upper and lower pool is constant. d) Top view of the setup: two copper meshes with different lengths of the horizontal sections (l_1 and l_2) are placed side by side. Two side by side mesh siphons are considered in each setup. The samples have the same length in the vertical sections but different lengths in the horizontal sections. Comparison of the resistance between the two samples allows approximate isolation of resistance due to the excess horizontal section in the longer sample (L^*).

experiment, 20 mL and 10 mL of water was dispensed into each top and bottom polypropylene reservoir, respectively. The saturated meshes were then placed on the holders, as seen in Figure 2a.

Each experiment was run for 24.0 ± 0.1 h, after which each pool's mass was measured using an analytical balance. Before starting an experiment, the mass of the copper mesh was weighed dry and after saturating the mesh with water. The difference between these masses yielded the mass of the water the mesh could hold in a saturated condition ($m_{\text{saturated}}$). Water was transferred from the upper pool to the lower pool by siphoning via capillarity of the mesh. The difference in mass at the lower pools from start to finish of an experiment was the mass transferred through wicking ($m_{\text{capillary}}$). $m_{\text{saturated}}$ was on average $\approx 7\%$ of $m_{\text{capillary}}$, which ensured that the primary transport of mass from the upper pool to the lower pool was by capillary wicking, and not draining of the mesh. The mass flow rate was calculated by the mass transferred divided by the time of the experiment and was converted to the volume flow rate by dividing by the density of water. The water evaporation was characterized from the upper and lower water pools by keeping them in the environment control chamber without the mesh installed between the pools for 24 h. The evaporation mass loss was $<5\%$ from all pools. A similar tracking of evaporation was done from saturated copper meshes by placing the meshes on a Teflon sheet inside the environment control chamber at 100% humidity for 24 h. The calculated mass loss due to evaporation from the saturated copper mesh was $<4\%$.

2.3.2. Maximum Capillary Pressure Measurement

For capillary rise measurements, a $4 \text{ cm} \times 30 \text{ cm}$ section was cut from the stock copper mesh described in Section 2.1. The section was cleaned following the procedure described in Table 1.

The experiment was conducted in an environmental control chamber to ensure that temperature and humidity remained constant during the duration of the experiment. Figure 3a gives a schematic of the set-up. An initially fully saturated mesh sat vertically in a pool of DI water. Water drained from the mesh and reached an equilibrium height. After 24 h, the height of the capillary rise, h_{max} , was recorded (Figure 3b). The maximum capillary pressure $P_c(\text{max})$ was given by $\rho g h_{\text{max}}$ where, ρ = density of water at 25°C , and g = gravitational acceleration.

2.3.3. Calculation of Permeability Thickness Product

To obtain a correlation between capillary pressure and permeability, the horizontal region of the sample where capillary pressure is not affected by gravity, was isolated (though it was still influenced by viscous loss as discussed below). Resistance to flow could be expressed as the driving force for flow divided by the flowrate. Thus, we could write the volumetric flow rate as,

$$Q = \frac{\text{driving force, that is, pressure differences}}{\text{resistance to flow}} \quad (2)$$

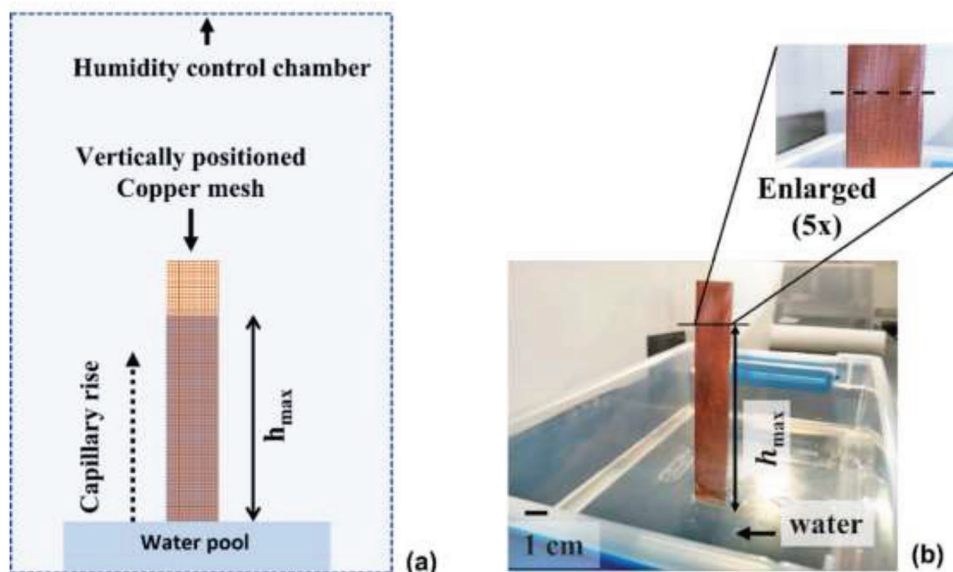
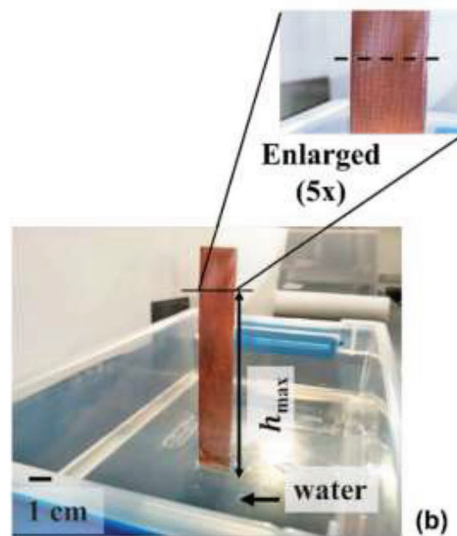


Figure 3. a) Schematic of capillary rise test experimental set-up. Saturated copper mesh stands vertically with one end dipped in a water pool and the other open to ambient. Set-up is enclosed in the chamber maintaining a fixed temperature and $\approx 100\%$ humidity during the experiment. b) Water drains from the saturated mesh and reaches an equilibrium at maximum capillary height, h_{\max} .

The pool height difference (driving force) was kept constant during all measurements. By changing the length of the horizontal section of the mesh, l_x , the resistance to flow was changed. For example, increasing l_2 to $l_2 + L^*$ (Figure 2) increased the resistance to flow of water through the mesh. This increase in resistance to flow resulted in a decreased volumetric flow rate to the lower pool. Thus, the resistance to flow could be quantified by measuring the volumetric flow rate at $l_2 + L^*$. This resistance and Darcy's law could be then used to determine the permeability thickness product ($k\delta$). The liquid pressure dropped along the length of the wick due to viscous loss. Capillary pressure, P_c , was defined as the difference between the gas pressure in the environment, P_g , and the local liquid pressure in the wick, P_l ($P_c = P_g - P_l$). Capillary pressure varied throughout the wick due to elevation change and viscous pressure loss. Two meshes were used side by side, having equal vertical wicking lengths but different horizontal flow lengths, to correct for the variable capillary pressure and permeability found in the vertical sections. The vertical sections of the mesh could be changed (e.g., $l_u + y$, from upper pool; $l_l + y$, from lower pool) to drive flow at varying capillary pressure. Resistance to flow for three mesh sections was defined, (l_u, l_x, l_l) to develop the calculation for determining permeability thickness product ($k\delta$) with different capillary pressure.

Figure 4 schematically shows the experimental set-up with corresponding resistances defined. Flow resistance for the shorter sample (A) was divided into: R_1 , related to the length of l_u ; R_2 , related to the length of l_2 , and R_3 , related to the length of l_l . Since all these resistances to flow were in series, the total resistance to flow of (A) could be written as $R_A = R_1 + R_2 + R_3$. Resistances for the longer sample (B) were similar to (A), except for the horizontal resistance which was $R_2 + R^*$, related to the length of $l_2 + L^*$. Thus, the total resistance to flow of (B) was $R_B = R_1 + R_2 + R^* + R_3$.



If R_A was subtracted from R_B , the resistance R^* related to the length L^* could be found, that is, $R^* = R_B - R_A$. Now, resistance to flow in B, $R_B = \frac{\text{driving force, that is, capillary pressure}}{Q}$. If V_B was the volume of water transferred in time Δt then, $Q = (V_B/\Delta t)$, and the driving pressure was ρgh , where ρ is the density of water at 25°C , g is gravitational acceleration, and h is pool height difference. Thus, $R_B = (\rho gh \Delta t/V_B)$. Similarly, $R_A = (\rho gh \Delta t/V_A)$. Therefore,

$$R^* = (\rho gh \Delta t/V_B) - (\rho gh \Delta t/V_A) \quad (3)$$

Again, if the flow of water was considered in the horizontal section of the mesh, it followed Darcy's law. For a mesh cross-sectional area of A , where $A = \text{width}(w) \times \text{thickness}(\delta)$, the volume flow rate, $Q = uA$. The resistance to flow R^* of the length L^* = pressure drop along the length $L^*/$ volume flow rate.

Or, $R^* = \Delta p/Q = \Delta p/uA = u \times \mu \times L^*/u \times k\delta w$, where, μ is the dynamic viscosity of the fluid.

Therefore, resistance to flow in the horizontal section with length L^* was,

$$R^* = \mu L^*/k\delta w \quad (4)$$

From (3) and (4), the thickness permeability was product given by:

$$\kappa\delta = \frac{\mu L^*}{w\Delta t(\rho gh)(1/V_B - 1/V_A)} \quad (5)$$

As the mesh was free standing, this product was considered to be the most appropriate measure of fluid conductivity for the structure.

Capillary pressure corresponding to the flow resistance measured (i.e., in the excess horizontal length, L^*) was not uniform

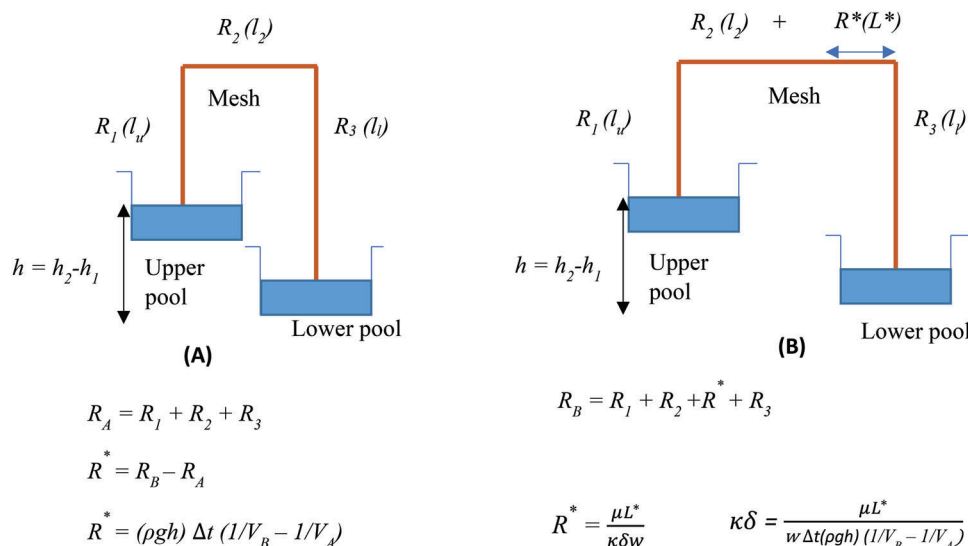


Figure 4. Calculation details to determine permeability thickness product ($k\delta$) at varying capillary pressures (P_c). δ is thickness, and w is width of the copper mesh. In (a), R_1 is resistance to flow of water in the part of length of l_u , R_2 is resistance to flow of water in the part of length of l_2 , and R_3 is resistance to flow of water in the part of length of l_1 . In (b), R^* is resistance to the flow of water in the length of L^* . h is the pool height difference between the upper and lower water pools. R_A is the total resistance to flow in setup (A) and R_B is the total resistance to flow in setup (B), $R^* = R_B - R_A$.

due to the viscous pressure loss in this section. This increment in viscous loss and corresponding capillary pressure also made the equivalence in resistance of the two samples' common sections (Figure 4) only approximate. The additional resistance induced some change in the capillary pressure and corresponding resistance of the remainder of the sample, but as shown in materials section, Supporting Information SM.(I), this contribution is relatively small. Viscous loss in the vertical and common horizontal sections also contributed uncertainty in the capillary pressure experienced by the section of interest (L^*). Here the capillary pressure was approximated at the region of interest as the average of the gravitational head above the upper and lower pools, that is, $P_c = \rho g \left(\frac{h_u + h_l}{2} \right)$. Approaches to eliminating this uncertainty in capillary pressure are discussed in the following section.

2.3.4. Scope and Limitations of Method

The method described here can be extended to measure permeability-capillary pressure relationships for a wide range of thin, porous structures. Forming the material of interest into the three sections of the measurement apparatus, as shown above, was convenient but not necessary and might not be possible for brittle materials. A separate standardized wicking material could be used for all but the unique section (L^* in Figure 2). The wicking material had to support a maximum capillary pressure higher than that of the material under test and preferably had low net flow resistance (which can be reduced by increasing thickness). A schematic of this modified approach is given in the Supporting Information SM.(IV).

The primary limitation in the method presented was the determination of capillary pressure at the section of interest. As discussed above, viscous pressure drop introduced uncertainty in the capillary pressure. Capillary pressure uncertainty was

bounded by the driving force applied for flow. A small height difference between upper and lower pools yielded well defined capillary pressure but also incurred low flow rates and attendant issues including increased importance of evaporation, liquid volume held in the mesh, and mass measurement uncertainty. Alternatively, the capillary pressure at the region of interest could be refined by an iterative approach applying the permeability-capillary pressure relation determined using the nominal capillary pressure to correct for viscous pressure drop, then rescaling the relation by the corrected capillary pressure and iterating until a self-consistent solution was obtained. Viscous pressure loss across the region of interest (L^*) also reduced the accuracy of equating the resistances of the remaining sections of both samples. This inaccuracy could be reduced by minimizing the length of the region of interest at the expense of reducing the difference in response between the samples and increasing error associated with the subtraction of the accumulated flows.

3. Statistical Analyses

We measured permeability of three independent samples at each capillary pressure. Data for all samples is presented. There is negligible uncertainty in the measured mass of liquid transferred and time for flow, which contribute to each permeability measurement. Maximum capillary pressure is determined from measurements of three independent samples. The average maximum capillary pressure and uncertainty, equal to the maximum difference between measured values and the average, are reported. There is negligible uncertainty in the height of the horizontal sections with respect to both pools from which the nominal capillary pressure is calculated. Ambiguities in capillary pressure associated with viscous pressure drop are discussed in the previous section.

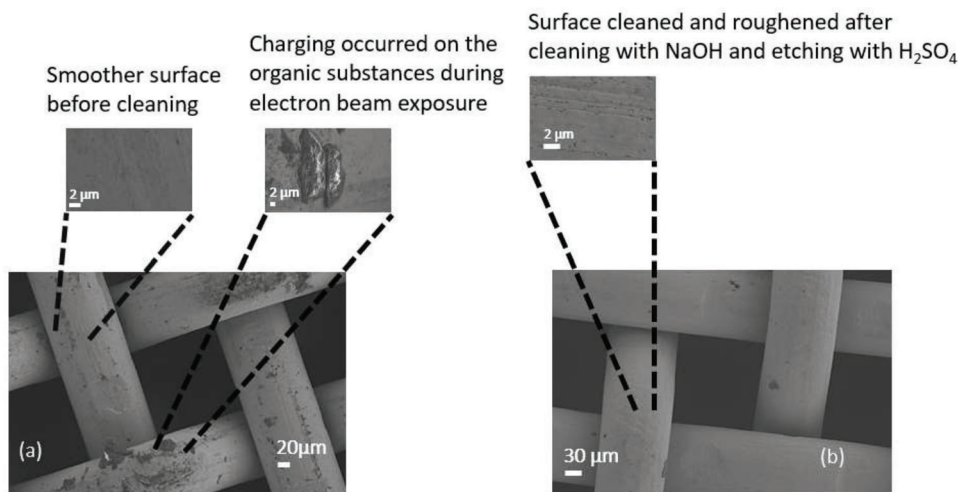


Figure 5. SEM of copper wire mesh surface: a) as received copper mesh contains organic compounds. Charging occurred on the organic substance on copper mesh during electron beam exposure. b) After cleaning with 1 M NaOH, the organic debris were removed from the surface and followed by etching with 1% H_2SO_4 further cleaned and roughened the copper mesh surface.

4. Results and Discussion

4.1. Surface Cleaning of Copper Wire Mesh

Based on SEM analysis, prior to surface cleaning, the mesh shows non-metallic debris on the wire surfaces, **Figure 5a**. This debris, which likely originates from the lubricant used during the drawing process of the copper wire as well as handling and storage of the mesh, agglomerates as islands on the surface of the mesh. It is detectable by electron beam charging. Following cleaning process steps 1–5 described above, the islands of debris are removed from the surface, **Figure 5b**. The surface of the copper mesh is again imaged after cleaning steps 6–9 (including etching in sulfuric acid). The etching results in roughening of the copper wire surface.

4.2. Maximum Capillary Pressure P_c (max)

Based on the method described above, the maximum capillary rise is measured as $h_{\max} = 10.5 \pm 0.2$ cm. The maximum capillary pressure supported by the mesh is determined as $P_c(\max) = h_{\max} \times \rho \times g = 1027 \pm 19.5$ Pa, where ρ is the density of water at 23 °C, and g is the gravitational acceleration.

4.3. Change of Permeability Thickness Product of Wire Mesh (#100) with Capillary Pressure

Using the procedure described above (Sections 2.3.1 and 2.3.3), we measure the permeability thickness product ($k\delta$) for the mesh over a range of capillary pressures from ≈ 600 Pa to ≈ 1000 Pa.

Figure 6 shows the permeability thickness product data for cleaned copper #100 mesh at different capillary pressures. We performed three independent $k\delta$ measurements for each capillary pressure with separate mesh samples for each measurement. The permeability thickness product is relatively insensitive

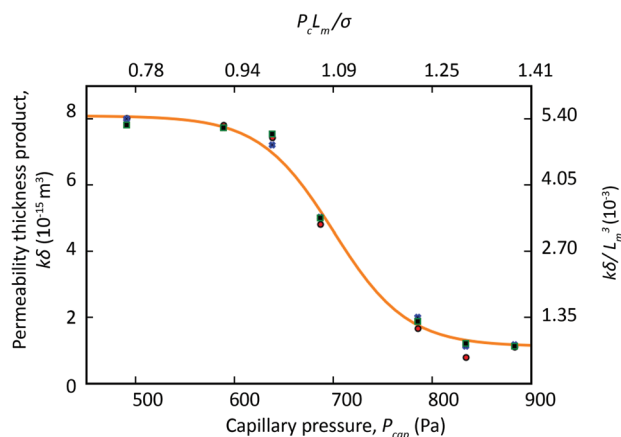


Figure 6. Permeability thickness product ($k\delta$) of plain weaved copper wire mesh #100 at different capillary pressures for water at room temperature. Data points are measured experimentally. Line is fit using Equation (6). Axes are also given for dimensionless flow resistance $k\delta/L_m^3$ (right) and dimensionless capillary pressure, $P_c L_m/\sigma$ (top). We used known surface tension of DI water at room temperature and wire diameter of the mesh to nondimensionalize the axes. Data for all (3) independent samples at each capillary pressure are shown.

to pressure at low capillary pressure. As we increase the capillary pressure, the $k\delta$ product value starts to decrease gradually at capillary pressures around 750 Pa. With an increase in capillary pressure the radius of curvature of the meniscus between the liquid and vapor phases decreases. For a free-standing mesh with two liquid-vapor interfaces at the top and bottom of the mesh, this results in a decreased cross section of liquid volume available for flow. $k\delta$ then decreases more rapidly with increasing capillary pressure, before the decrease moderated around 950 Pa. At even higher capillary pressures, beyond 1000 Pa, the $k\delta$ value is very low and again shows relative insensitivity to capillary pressure. We fit (orange curve of **Figure 6**) the permeability thickness

product versus capillary pressure data with a sigmoidal curve as chosen below, where P_c is capillary pressure.

$$k\delta = \frac{a}{1 + \exp(b(P_c - c))} + d \quad (6)$$

A least squares regression yields the following parameters: $a = 7.07 \times 10^{-15} \text{ m}^3$, $b = 0.0208 \text{ Pa}^{-1}$, $c = 700 \text{ Pa}$, $d = 1.11 \times 10^{-15} \text{ m}^3$. We note that this fit does not have a physical basis, and other functions could be applied. The experimental uncertainty of the experimental data may originate from different surface conditions of the copper mesh originating from the mesh processing step, different rates of evaporation of water during experiments, and deviation from linearity in the vertical and horizontal sections of the mesh originating from the mesh folding step. The masses of the water pools were measured using an analytical balance and likely do not contribute appreciably to experimental uncertainty.

We have considered simple porous flow resistance models for comparison to the measured mesh behavior at low capillary pressure. The Carman–Kozeny relationship predicts a value of $k\delta = 45.3 \times 10^{-15} \text{ m}^3$ ($k\delta = (D_p^2/180) \times (\phi^3/(1 - \phi)^2) \times \delta$, where, D_p is the effective pore size of the mesh, and Φ is the porosity of the copper mesh.^[15] For our copper mesh the calculated porosity Φ is 65% (see SM.(III), Supporting Information). As expected, such a calculation which attributes the full thickness of the mesh as available to flow, overestimates the observed flow (e.g., by $\approx 400\%$).

We note that the hydrodynamic pressure drops along the horizontal length of the wick for the flow rates measured through our experiment is small compared to the mean capillary pressure. The ratio of the pressure drops (ΔP) to the capillary pressure (P_c) ranged between 16% to 21% (Figure SM1, Supporting Information).

4.4. Dimensional Analysis

The results obtained for flow resistance versus capillary pressure for the free-standing mesh can be generalized beyond the specific size and material of mesh studied. Dimensional analysis allows us to consider the relationship between non-dimensionalized expressions of flow resistance and capillary pressure, which can be applied to similarly shaped meshes of different scales.

For small meshes of similar geometry but different scale (i.e., plain weave meshes with the same ratio of wire diameter to opening size), we can expect the value of $k\delta$ to depend only on a limited number of parameters. These are L_m , length scale of the mesh (e.g., diameter of the mesh wire or mesh spacing), σ , surface tension of the liquid, P_c , capillary pressure, and liquid contact angle for the surface, θ . Only these parameters are significant as long as surface tension dominates. For the mesh considered here, the Bond (or Eötvös) number ($\frac{\Delta\rho g L^2}{\sigma}$) is very small. Using the wire diameter as the characteristic length, the calculated Bond number is $1.75 \times 10^{-3} \ll 1$, indicating that the surface tension forces overwhelm gravitational ones. Furthermore, the fluid is in the Stokes flow regime (Reynold's number, $Re < 5 \times 10^{-4}$ at room temperature for water) so that we can define a flow resistance that is independent of the effect of fluid veloc-

ity and driving pressure for flow. We further note that many liquid/solid combinations will have a contact angle near zero. For example, clean solid metal surfaces are hydrophilic and tend to have very low contact angle with water (close to 0-degree). Based on Hamaker coefficients for metal surfaces using Lifshitz theory, it is suggested that physical interactions at the metal–water interface are composed solely of dispersion forces. If the macroscopic Hamaker coefficients are calculated from the Lifshitz theory, dispersion forces alone are sufficient to predict metal surfaces as strongly hydrophilic.^[23,42–45] Furthermore, low surface tension liquids such as hydrocarbons or halogenated hydrocarbons show essentially zero contact angle on many surfaces.

From dimensional analysis we find that,

$$k\delta/L_m^3 = f'(P_c L_m/\sigma, \theta) \quad (7)$$

where L_m , length scale of the mesh (e.g., diameter of the mesh wire, mesh spacing, or mesh opening), σ , surface tension of the liquid, P_c , capillary pressure, and liquid contact angle for the surface, θ .

Equation (7) is a generalized non dimensional one, that can be used along with the plot in Figure 6 to describe flow resistance of meshes with any mesh number that have a similar weave (i.e., geometric similarity) as that described in Section 2.1, and liquid/solid combination with similar contact angle. Figure 6 also shows axes for nondimensionalized capillary pressure, $P_c L_m/\sigma$, (top) and flow resistance, $k\delta/L_m^3$, (right). Details of the dimensional analysis are given in the Section SM.(II), Supporting Information.

4.5. Effect of Surface Cleaning

We measured the permeability of as-received copper mesh containing surface debris, without surface cleaning. We find the permeability of the as received mesh is lower than the cleaned copper mesh at a similar capillary pressure (e.g., at $\approx 490 \text{ Pa}$ the permeability thickness product of as received mesh prior to cleaning is $\approx 2.2 \times 10^{-15} \text{ m}^3$ compared to $\approx 8.1 \times 10^{-15} \text{ m}^3$). We believe this effect results from poor wetting of the mesh by water due to non-polar nature of the potential contamination, such as oil. We also measured the wetting property of the as-received mesh prior to cleaning by a capillary rise test with DI water as our working fluid in a humid environment. After 24 h we find that the maximum capillary height on the uncleaned mesh is, $h_{\max}^{\text{uncleaned}} = 3.8 \text{ cm}$, and the resulting maximum capillary pressure of the uncleaned mesh $P_c(\max_{\text{uncleaned}}) = h_{\max}^{\text{uncleaned}} \times \rho \times g = 371 \text{ Pa}$.

4.6. Flow Performance of Free-Standing Meshes

The permeability/capillary pressure relation given in Figure 6 provides information necessary to predict flow through free standing meshes having various lengths and applied driving pressure. This can be expressed in general form as an integration of Darcy's law for pressure drop along one dimension (the flowline). The volumetric flow rate of a free-standing mesh, normalized by the viscosity of the liquid and the length of the mesh,

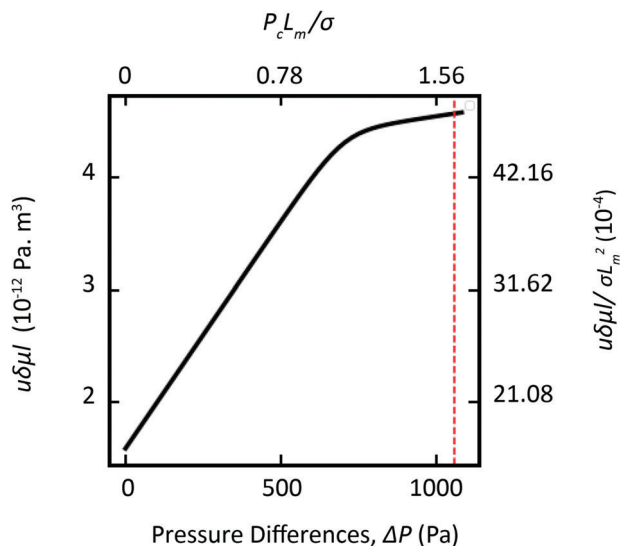


Figure 7. Normalized superficial velocity $u\delta\mu l$ (Pa m^3) versus pressure differences ΔP (Pa). We used wire diameter and surface tension of DI water at room temperature to nondimensionalize the axes. The red-dotted straight line indicates the maximum capillary pressure, P_c (max).

can be described using a modified version of Darcy's law as follows:

$$u\delta\mu l = \int_0^P \kappa \delta (p_g - p) dp \quad (8)$$

where p_g is the vapor pressure and p is the liquid pressure. For a constant gas pressure surrounding the free-standing, horizontal mesh, the capillary pressure increases proportionally to the hydrodynamic pressure loss. We determine the $\kappa\delta(p)$ relationship from our experiments, as fit in Equation (6). Applying this relationship, assigning zero capillary pressure at zero position, and integrating with respect to pressure in the liquid gives us the superficial velocity of water in a 1D free-standing wick normalized with regards to viscosity and length of the wick.

The integration of Equation (8) yields,

$$u\delta\mu l = (a + d) \Delta P - \frac{a}{b} \ln(e^{b(\Delta P - c)} + 1) + p_0 \quad (9)$$

where $p_0 = 5.07 \times 10^{-12} \text{ Pa m}^3$ (values of other constants are given above with Equation (6)) Plotting Equation (9) for different pressure differences (ΔP), we find that the normalized superficial velocity ($u\delta\mu l$) increases with increasing pressure difference almost linearly at lower pressures. After a specific pressure drop, the rate of change of $u\delta\mu l$ decreases significantly, corresponding to the increase in flow resistance with increasing capillary pressure. Following the dimensional analysis approach above, we can likewise relate a dimensionless velocity length product and pressure (Figure 7).

Equation (9) can be applied to understand the performance of mesh in specific cases. We can consider the maximum flowrate that can be achieved for DI water in copper #100 mesh with plain weave and wire diameter 0.114 mm assuming a driving pressure equal to the maximum capillary pressure. Figure 8a shows the values of superficial velocity through a single layer free standing mesh wick, $u\delta$, at maximum driving pressure for different dy-

namic viscosities, 0.282 mPa s, 0.354 mPa s, 0.466 mPa s, 0.6527 mPa s, and 0.95 mPa s, respectively. For a fixed capillary pressure, $u\delta$ decreases with increasing wicking length asymptotically approaching zero at rates determined by the liquid viscosity. Likewise, Figure 8b shows $u\delta$ in the mesh at wicking lengths of $l = 0.25 \text{ cm}$, $l = 0.50 \text{ cm}$, $l = 0.75 \text{ cm}$, and $l = 1 \text{ cm}$ versus total pressure drop for DI water (dynamic viscosity at boiling point of water, $\mu = 0.282 \text{ mPa s}$), demonstrating higher $u\delta$ through shorter wicking distance with increasing pressure differences.

Furthermore, we consider the nondimensionalized version of Equation (9) (see the Section SM.(II)'s Equation (SM2), Supporting Information) to evaluate the performance of two common fluids used in electronics cooling applications HFO1233zd (at 25 °C surface tension, $\sigma = 12.57 \text{ mN m}^{-1}$ and dynamic viscosity, $\mu = 0.469 \text{ mPa s}$, $\theta \approx 0^\circ$) and HFE7100 (at 25 °C surface tension, $\sigma = 13.345 \text{ mN m}^{-1}$ and dynamic viscosity, $\mu = 0.58 \text{ mPa s}$, $\theta \approx 0^\circ$), in plain weaved single layer copper #100 mesh with 0.114 mm wire diameter.^[46–48] Figure 9a shows the values of $u\delta$, at maximum driving pressure for dynamic viscosities of 0.469 mPa s (HFO1233zd) and 0.581 mPa s (HFE7100). Due to the lower surface tension of these fluids than DI water at similar temperature, the maximum driving force (pressure difference) we can apply is significantly lower than that of DI water. Figure 9b shows the behavior of $u\delta$ for HFO1233zd and HFE7100 in #100 mesh at wicking lengths of $l = 0.25 \text{ cm}$. $u\delta$ increases with driving pressure differences (There is a marginally higher P_c (max) for HFO1233zd than HFE7100).

4.7. Comparison among Methods to Measure Permeability of Mesh Geometries

Table 2 provides a comparison of permeability measurement methods and models applied to various mesh geometries. These include methods correlating flow and pressure drop^[24,25,31] and rate of liquid imbibition into unsaturated samples.^[49] We note that most methods are not suitable for measuring permeability-capillary pressure relationships. The method of Si Cong Tan et al., used to measure the permeability-capillary pressure relationship of a thin mesh welded on a thin sheet, is an exception. However, this method cannot be easily modified to measure the permeability of a free-standing mesh where the mesh is exposed to liquid-vapor interface on both sides. The rate-of-rise method^[1] is readily applied to free standing mesh structures. However, we note that there is ambiguity in comparing the rate-of-rise method, that determines the velocity of a saturation front, and the current method, that measures flow rate. A direct comparison requires a known cross-section for liquid flow, which is not precisely defined for free standing meshes, as discussed above. Additionally, the mesh considered here shows dramatic asymmetry in the rate of imbibition and drainage, as do various other porous materials, making the interpretation of rate of rise measurements ambiguous in these cases. The rate of rise method also does not provide direct information on capillary pressure dependence.

4.8. Validation of Method

To validate the method described in this work, we compare the permeability of Whatman 1 filter paper at low capillary pressure

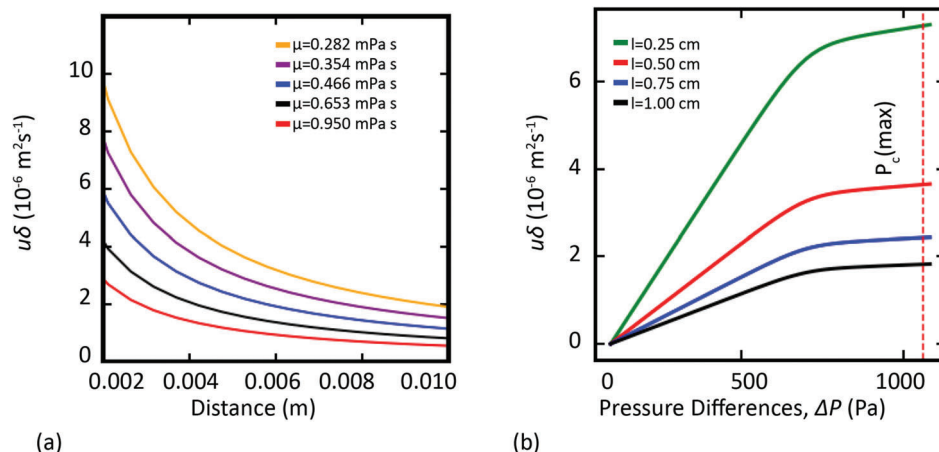


Figure 8. a) Superficial velocity through a single layer free standing mesh wick, $u\delta$ ($\text{m}^2 \text{ s}^{-1}$), decreases with increasing wicking distance at maximum capillary pressure. Longer wicking lengths experience more considerable viscous drag compared to shorter wicking lengths. $u\delta$ of DI water is thus lower for longer wicking lengths than that of shorter wicking lengths. b) $u\delta$ ($\text{m}^2 \text{ s}^{-1}$) versus pressure difference, ΔP (Pa), at different wicking lengths. The red-dotted straight line indicates the maximum capillary pressure, P_c (max).

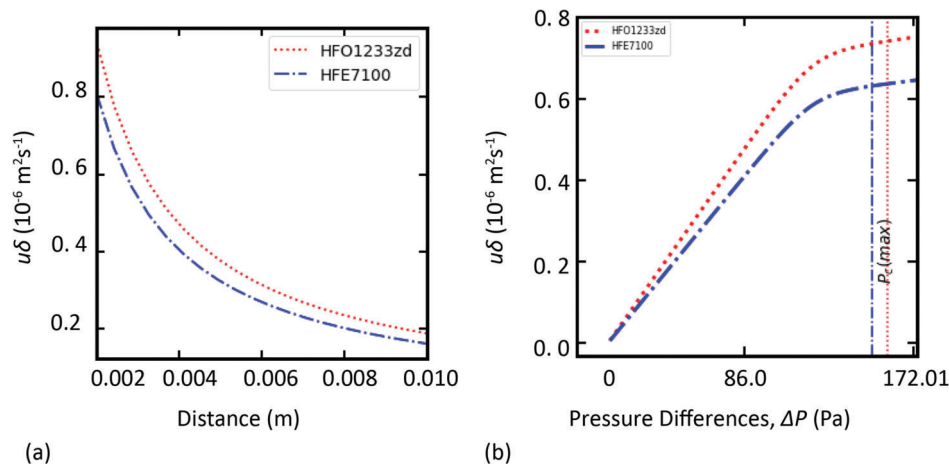


Figure 9. a) $u\delta$ ($\text{m}^2 \text{ s}^{-1}$) with increasing wicking distance at maximum capillary pressure for common fluids used in electronics cooling application (HFO1233zd and HFE7100, respectively). b) $u\delta$ ($\text{m}^2 \text{ s}^{-1}$) versus pressure difference, ΔP (Pa), at wicking length of $l = 0.25$ cm for HFO1233zd and HFE7100, respectively. The red-dotted straight line indicates the maximum capillary pressure, P_c (max) of HFO1233zd. The blue-dotted straight line indicates the maximum capillary pressure, P_c (max) of HFE7100.

obtained using a variety of approaches. We measure a permeability of $1.72 \times 10^{-13} \text{ m}^2$ using the method presented here. Using the rate-of-rise method^[1] on the Whatman 1 filter paper, we measure a permeability of $1.96 \times 10^{-13} \text{ m}^2$. From the Herzberg number provided by the supplier^[52] (100 mL/150 s) we calculate the permeability as $1.57 \times 10^{-13} \text{ m}^2$. These permeability values are also consistent with the existing literature data on permeability of Whatman 1 filter paper: $1.41 \times 10^{-13} \text{ m}^2$ in ref. [33] and $2.01 \times 10^{-13} \text{ m}^2$ in ref. [53]. Details of the permeability measurements conducted on filter paper are discussed in Section SM.(V), Supporting Information.

5. Conclusions

We proposed and demonstrated a novel and simple experimental technique that can be used to measure the permeability of free-standing mesh wicks with liquid–vapor interfaces on both

sides of the wicks. Our experimental approach used water pools at different heights to create a driving force based on gravitational potential, allowing for liquid capillary suction through the mesh. To ensure accurate results, a surface cleaning protocol was established to clean the surfaces of the copper mesh from any organic debris. The meshes were thoroughly saturated with deionized (DI) water before the experiments and operated in the drainage regime. To determine the maximum capillary pressure obtained from the metal meshes, a capillary rise test was conducted. Additionally, an environmental control chamber was used to conduct the experiments at 100% relative humidity to eliminate any effect of evaporation on the measurements. Importantly, this method does not require visual monitoring or a micropump for fluid flow, making it a cost-effective and efficient way to measure the permeability of mesh wicks.

Furthermore, this accessible set-up method couples the permeability with capillary pressure in mesh wicks. We report the

Table 2. Methods for measuring and calculating permeability for different mesh geometries..

Method/geometry	Mesh number	Reported permeability [m ²]	Applicable to free standing mesh	Capillary pressure dependence	Ref.
Flow with micropump/single-layer mesh welded on plate ^{a)}	150	2.2×10^{-11}	No	Yes	[31]
Gravity flow/stacks of mesh ^{b)}	150	5×10^{-11}	No	No	[24, 25]
Capillary rate of rise/single-layer mesh welded on grooved plate	200	9.57×10^{-11}	Yes	No	[49]
Capillary rate of rise/two meshes stacked and sintered on plate	200	1.91×10^{-11}	Yes	No	[49]
Mathematical formula/ <i>N</i> layers of mesh ^{c)}	Variable	Variable	No	No	[50]
Rate of rise/single layer Dutch twill weave mesh	200/1400	Warp = 0.73×10^{-12} Weft = 0.36×10^{-12}	Yes	No	[51]
Siphon/gravity flow/single-layer free-standing mesh ^{d)}	100	2.85×10^{-11}	Yes	Yes	This work

^{a)} Data for other mesh sizes #200, #250 with varying wire diameters 30,40,50 microns are also presented. Mesh material: Copper; ^{b)} Data for other mesh sizes are also presented in.^[25,26] Mesh materials: Stainless steel, phosphor bronze; ^{c)} The formula for stacks of mesh; ^{d)} Using mesh thickness of 0.280 mm for δ .

change in permeability with capillary pressure in single layer free-standing mesh like structure by a correlation equation. The wicks show an essentially bistable response to capillary pressure. Flow resistance is essentially constant at low capillary pressures, then increases dramatically before stabilizing at high capillary pressure. We consider the generalization of these results to plain weave meshes of other scales and different fluids by dimensional analysis. We also calculate the flow behavior of meshes under specific conditions based on the observed flow resistance/capillary pressure relationship and the integration of Darcy's law. By integrating Darcy's law, we calculated the flow velocity profile of DI water in metal mesh wicks using the correlation function we found through our experiment. The superficial velocity of water in copper mesh increases linearly until, at higher capillary pressures, the velocity increase goes down. At maximum capillary pressure, the superficial velocity of water decreases hyperbolically as the meniscus travels along the wicking length. The nondimensionalized permeability–capillary pressure relationship can be used to understand these materials' properties for any mesh sizes with similar weave and materials.

The methods and observations discussed are vital for designing and synthesizing devices that use single-layer, free-standing mesh structures for applications in which the permeability of the structures is affected by capillary pressure. These applications include two-phase heat transfer for electronics cooling, electrochemical energy conversion devices, and deionization cells for water purification.

Supporting Information

Supporting Information is available from the Wiley Online Library or from the author.

Acknowledgements

This research was supported by funding from the Advanced Research Projects Agency-Energy (ARPA-E), an agency of the U.S. Government, U.S. Department of Energy, under Award Number DE-AR0001055 in the OPEN

program monitored by Dr. Peter de Bock. The authors acknowledge the Imaging and Microscopy Facility (IMF) at UC Merced (funded under NSF EAR Award number: 0420982) for use of the SEM instrument. M.S. would like to thank Kennedy Nguyen for helpful discussions on electron microscopy. Additionally, M.S. appreciates Brandon Yang, Carson Whitt, George Montross, Kamila Ramirez, Carlos Cruz, and Amani Byron for their help with sample preparation; and Qianying Wu for help with literature search. This paper's views, opinions, and findings are those of the authors. This work was co-authored by the National Renewable Energy Laboratory (NREL), operated by Alliance for Sustainable Energy, LLC, for the U.S. Department of Energy (DOE) under Contract No. DE-AC36-08GO28308. This work was supported by ARPA-E funding. The views expressed in the article do not necessarily represent the views of the DOE or the U.S. Government. The U.S. Government retains and the publisher, by accepting the article for publication, acknowledges that the U.S. Government retains a nonexclusive, paid-up, irrevocable, worldwide license to publish or reproduce the published form of this work, or allow others to do so, for U.S. Government purposes.

Conflict of Interest

The authors declare no conflict of interest.

Data Availability Statement

The data that support the findings of this study are available from the corresponding author upon reasonable request.

Keywords

Darcy's law, dimensional analysis, free standing mesh, maximum capillary pressure, permeability measurement, porous media

Received: April 22, 2023
Revised: June 27, 2023
Published online: July 24, 2023

- [1] B. Holley, A. Faghri, *Appl. Therm. Eng.* **2006**, 26, 448.
[2] C. Salameh, D. Voiry, *Nat. Mater.* **2022**, 21, 1106.

- [3] J. Shen, Y. Cai, C. Zhang, W. Wei, C. Chen, L. Liu, K. Yang, Y. Ma, Y. Wang, C.-C. Tseng, J.-H. Fu, X. Dong, J. Li, Xi-X Zhang, L.-J. Li, J. Jiang, I. Pinnau, V. Tung, Yu Han, *Nat. Mater.* **2022**, 21, 1183.
- [4] D. Salvatori, B. Caglar, H. Teixidó, V. Michaud, *Composites, Part A* **2018**, 108, 41.
- [5] D. May, A. Aktas, S. G. Advani, D. C. Berg, A. Endruweit, E. Fauster, S. V. Lomov, A. Long, P. Mitschang, S. Abaimov, D. Abliz, I. Akhatov, M. A. Ali, T. D. Allen, S. Bickerton, M. Bodaghi, B. Caglar, H. Caglar, A. Chiminelli, N. Correia, B. Cosson, M. Danzi, J. Dittmann, P. Ermanni, G. Francucci, A. George, V. Grishaev, M. Hancioglu, M. A. Kabachi, K. Kind, et al., *Composites, Part A* **2019**, 121, 100.
- [6] J. W. Palko, C. Zhang, J. D. Wilbur, T. J. Dusseault, M. Asheghi, K. E. Goodson, J. G. Santiago, *Appl. Phys. Lett.* **2015**, 107.
- [7] C. Zhang, J. W. Palko, M. T. Barako, M. Asheghi, J. G. Santiago, K. E. Goodson, *Adv. Funct. Mater.* **2018**, 28, 1.
- [8] Y. Song, H. Cha, Z. Liu, J. H. Seong, L. Zhang, D. J. Preston, E. N. Wang, *Int. J. Heat Mass Transfer* **2022**, 185, 122320.
- [9] M. M. Rahman, M. Mccarthy, *J. Heat Transfer* **2017**, 139, 1.
- [10] M. M. Rahman, E. Ölçeroğlu, M. Mccarthy, *Langmuir* **2014**, 30, 11225.
- [11] C. Li, G. P. Peterson, Y. Wang, *J. Heat Transfer* **2006**, 128, 1312.
- [12] C. Li, G. P. Peterson, *J. Heat Transfer* **2006**, 128, 1320.
- [13] N. Lu, J. Li, Y. Sun, *Front. Heat Mass Transfer* **2022**, 18, 24.
- [14] C. Byon, S. J. Kim, *J. Micromech. Microeng.* **2011**, 21, 115011.
- [15] R. Schulz, N. Ray, S. Zech, A. Rupp, P. Knabner, *Transp. Porous Media* **2019**, 130, 487.
- [16] Youngsuk Nam, S. Sharratt, C. Byon, Sung Jin Kim, Y. S. Ju, *J. Microelectromech. Syst.* **2010**, 19, 581.
- [17] A. Wagner, E. Eggenweiler, F. Weinhardt, Z. Trivedi, D. Krach, C. Lohrmann, K. Jain, N. Karadimitriou, C. Bringedal, P. Volland, C. Holm, H. Class, H. Steeb, I. Rybak, *Transp. Porous Media* **2021**, 138, 1.
- [18] A. Faghri, Y. Zhang, *Transport Phenomena in Multiphase Systems*, Academic Press, Cambridge, MA **2006**, p. 331.
- [19] F. A. L. Dullien, *Porous Media: Fluid Transport and Pore Structure*, Academic Press, Cambridge, MA **1992**.
- [20] T. A. Ghezzehei, T. J. Kneafsey, G. W. Su, *Water Resour. Res.* **2007**, 43, 1.
- [21] P. Papatzacos, S. M. Skjæveland, in *Proc. – SPE Annual Technical Conf. and Exhibition*, Society of Plastic Engineers, San Antonio, TX **2002**, p. 1841.
- [22] J. D. Valiantzas, *J. Irrig. Drain. Eng.* **2011**, 137, 223.
- [23] L. Makkonen, *J. Chem. Phys.* **2017**, 147, 064703.
- [24] Y. Ikeda, in *Proc. of the Symp. on Mechanics for Space Flight* **1985**, Report SP No.3, 119.
- [25] H. Kozai, I. Imura, Y. Ikeda, *JSME Int. J.* **1991**, 34, 212.
- [26] H. Noda, K. Yoshioka, T. Hamatake, *JSME Int. J., Ser. B* **1993**, 36, 357.
- [27] B. Subedi, S. H. Kim, S. P. Jang, M. A. Kedzierski, *Int. J. Heat Mass Transfer* **2019**, 131, 537.
- [28] D. R. Adkins, R. C. Dykhuizen, *Proc. Intersoc. Energy Convers. Eng. Conf.* **1993**, 2, 911.
- [29] A. Arulselvan, N. Ramasubbu, V. Pandiyarajan, *AIP Conf. Proc.* **2019**, 2161, 020010.
- [30] J. H. Ambrose, L. C. Chow, J. E. Beam, *J. Thermophys. Heat Transfer* **1990**, 4, 318.
- [31] S.-C. Tan, C. Guo, Y.-Y. Jiang, T. Wang, C.-Z. Li, *Int. Commun. Heat Mass Transfer* **2022**, 131, 105879.
- [32] G. Rong, J. W. Palko, D. I. Oyarzun, C. Zhang, J. Hämmerle, M. Asheghi, K. E. Goodson, J. G. Santiago, *J. Colloid Interface Sci.* **2018**, 530, 667.
- [33] S. Patari, P. S. Mahapatra, *Langmuir* **2022**, 38, 4736.
- [34] L. M. Skinner, J. R. Sambles, *J. Aerosol Sci.* **1972**, 3, 199.
- [35] F.-J. Granados-Ortiz, A. López-Martínez, F. D. Molina-Aiz, C.-H. Lai, A. Peña-Fernández, J. A. Martínez-Lao, D. L. Valera-Martínez, *Agronomy* **2023**, 13, 602.
- [36] F. A. L. Dullien, in *Porous Media*, 2nd ed., Academic Press, Cambridge, MA **1992**, p. 117.
- [37] H. J. Cho, D. J. Preston, Y. Zhu, E. N. Wang, *Nat. Rev. Mater.* **2016**, 2, 1.
- [38] F. A. L. Dullien, M. S. El-Sayed, V. K. Batra, *J. Colloid Interface Sci.* **1977**, 60, 497.
- [39] H. P. J. De Bock et al., in *Proc. of IMECE2008*, **2008**, 10, 991.
- [40] M. Shattique et al., in *APS March Meeting*, **2023**, Session K18, Fluids:VI.
- [41] E. M. Dede, C. Zhang, Q. Wu, N. Seyedhassantehrani, M. Shattique, S. Roy, J. W. Palko, S. Narumanchi, B. Kekelia, S. Hazra, K. E. Goodson, R. Giglio, M. Asheghi, *iScience* **2023**, 26, 105812.
- [42] M. E. Schrader, *J. Colloid Interface Sci.* **1984**, 100, 372.
- [43] D. Y. Kwok, D. Li, A. W. Neumann, *Colloids Surf., A* **1994**, 89, 181.
- [44] D. Y. Kwok, A. W. Neumann, *Adv. Colloid Interfaces Sci.* **1999**, 81, 167.
- [45] F. M. Fowkes, *J. Phys. Chem.* **1963**, 67, 2538.
- [46] R. J. Hulse, R. S. Basu, R. R. Singh, R. H. P. Thomas, *J. Chem. Eng. Data* **2012**, 57, 3581.
- [47] M. H. Rausch, L. Kretschmer, S. Will, A. Leipertz, A. P. Fröba, *J. Chem. Eng. Data* **2015**, 60, 3759.
- [48] S. N. Joshi, F. Zhou, Y. Liu, D. J. Lohan, H. Ukegawa, J. Lee, E. M. Dede, *IEEE Trans. Power Electron.* **2023**, 38, 6790.
- [49] S.-C. Wong, M.-S. Deng, M.-C. Liu, *Int. J. Heat Mass Transfer* **2022**, 184, 122259.
- [50] A. Faghri, *Heat Pipe Science and Technology*, Taylor & Francis Ltd., Milton Park, Oxfordshire **1995**.
- [51] N. Fries, K. Odic, M. Conrath, M. Dreyer, *J. Colloid Interface Sci.* **2008**, 327, 118.
- [52] G. E. Healthcare and Life Sciences, “Laboratory filtration Principles and chemical compatibility chart,” **2013**, 29-0461-71 AA 03/2013.
- [53] Z. Liu, J. Hu, Y. Zhao, Z. Qu, F. Xu, *Appl. Therm. Eng.* **2015**, 88, 280.